Applied Catalysis B: Environmental 218 (2017) 430–442

Contents lists available at ScienceDirect

Applied Catalysis B: Environmental

journal homepage: www.elsevier.com/locate/apcatb

Co-oxidation of CO and propylene on Pd/CeO_2-ZrO_2 and Pd/Al_2O_3 monolith catalysts: A light-off, kinetics, and mechanistic study

Wendy Lang[a], Paul Laing[b], Yisun Cheng[b], Carolyn Hubbard[b], Michael P. Harold[a,*]

[a] Department of Chemical and Biomolecular Engineering, Texas Center for Clean Engines, Emissions & Fuels, University of Houston, Houston, TX 77204, United States

[b] Research and Innovation Center, Ford Motor Company, Dearborn, MI 48124, United States

ARTICLE INFO

Article history:
Received 27 February 2017
Received in revised form 22 May 2017
Accepted 20 June 2017
Available online 21 June 2017

Keywords:
Palladium
Ceria
Three-way catalyst
Light-off
Oxidation
Carbon monoxide
Propylene

ABSTRACT

The light-off (ignition) and steady-state behavior for individual oxidation and co-oxidation of CO and propylene under near-stoichiometric conditions was studied using Pd/Al_2O_3 and Pd/CeO_2-ZrO_2 monolith catalysts. CO and propylene are shown to be self- and mutually-inhibiting, with inhibition mitigated by the promotional effect of CeO_2-ZrO_2. Oxidation is enhanced at low temperatures for CO, and at intermediate and high temperatures for propylene. Light-off behavior during CO and propylene co-oxidation is similarly improved at low and high temperatures. Steady-state differential kinetics measurements using Pd/Al_2O_3 show reaction orders of ~−1 with respect to CO and propylene. Using Pd/CeO_2-ZrO_2, the reaction order with respect to CO shifts towards zero and the activation energy decreases, suggesting an alternate reaction mechanism for CO oxidation when enough ceria is present. Mechanisms for CO and propylene oxidation that are consistent with the kinetics and inhibition trends are presented.

© 2017 Elsevier B.V. All rights reserved.

1. Introduction

Three-way catalysts (TWCs) are used in gasoline engine vehicles to reduce exhaust emissions of carbon monoxide (CO), hydrocarbons (HCs), and nitrogen oxides (NOx). TWCs are capable of converting the three exhaust pollutants to products CO_2, H_2O, and N_2. As federally-mandated emission and fuel economy standards become increasingly stringent, TWC light-off (LO) performance is critical in cost effectively meeting new and future regulations. Means of improving catalyst LO include catalyst modifications that minimize inhibition effects of exhaust species and optimization of precious group metal (PGM) loading.

TWCs consist of PGM dispersed on washcoated support materials loaded on cordierite monoliths. Palladium (Pd) is the main oxidation component in most modern automotive TWCs [1,2]. Its use in TWCs is incentivized by its superior thermal stability, a lower tendency to react with support materials (relative to base or non-noble metals), non-volatile oxides, and relatively lower cost and broader availability compared to Pt [1–3]. The type of catalyst support used affects the dispersion of precious metal sites, thermal stability of components, surface area, pore volume, and surface reactivity [4]. Mixed oxides including alumina (Al_2O_3), ceria (CeO_2), and zirconia (ZrO_2) are commonly used; Al_2O_3 provides a high surface area support and carrier for precious metal catalysts [4,5]. Al_2O_3 further helps bind the catalyst layer to the substrate (e.g. cordierite) and also absorbs poisons, helping retain catalyst performance [3].

To compensate for deviations from ideal stoichiometric three-way catalyst operating conditions, oxygen storage components are added to the catalyst, with ceria being the main oxygen storage component used today [1]. Ceria is incorporated in three-way catalysts because of its ability to be reduced and re-oxidized, cycling between the bounds Ce(3+) (Ce_2O_3) and Ce(4+) (CeO_2) to store oxygen, e.g. $Ce_2O_3 + 0.5O_2 \rightarrow 2CeO_2$ [3,6,7]. This redox chemistry and oxygen storage capacity enables the oxidation of CO and HCs under rich transient conditions [3]. Ceria also has a stabilizing effect on Al_2O_3 and precious metal dispersion [3,8,9]. Zirconia improves the activity and thermal stability of γ-Al_2O_3 and ceria, and has been shown to prevent the grain growth of ceria crystallites at high temperatures [5].

Pd/Ceria and Pd/Ceria-Zirconia (Pd/CZO) containing catalysts have been used and compared to conventional Pd/Al_2O_3 catalysts with promising results in ameliorating the self-inhibitory nature of CO and hydrocarbon oxidation [6–8,10–13]. LO under near ambient conditions is desired to reduce or overcome cold-start emissions;

* Corresponding author.
E-mail address: mharold@uh.edu (M.P. Harold).

http://dx.doi.org/10.1016/j.apcatb.2017.06.064
0926-3373/© 2017 Elsevier B.V. All rights reserved.

WRG-1013

and, using Pd/Ceria powder catalysts, LO of CO has been observed below 100 °C [8,14]. From a kinetics standpoint, incorporating ceria in PGM catalysts has been observed to increase the rate of CO oxidation and reaction order with respect to CO relative to conventional PGM/Al_2O_3 catalysts [6–10,11,15–17]. CO adsorbed on and covering the PGM surface can react with not only adsorbed and dissociated oxygen species (e.g. the oxidation mechanism on PGM/Al_2O_3), but also oxygen supplied by the ceria support, i.e. via an alternate mechanism that improves the overall rate of reaction [6–8,11,16–18]. This enhancement is attributed to the interfacial reaction between CO adsorbed on PGM active sites and oxygen supplied by ceria in the catalyst support [8,11,18]. The degree of enhancement using PGM/Ceria catalysts is dependent on the metal particle size (more specifically, the length of the interface between metal particles and the ceria support), whereas alumina-based catalysts exhibit rates independent of particle size [11,18]. Saturation of PGM sites by CO likely limits the effects of size-dependence for PGM/Al_2O_3 catalysts; however, CO on the metal does not impact the rate of O_2 adsorption onto ceria, and thus the higher the concentration of peripheral sites, the higher the rate of CO oxidation [11]. Self-inhibition of other exhaust species such as propylene, acetylene, and toluene have been observed using various PGM catalysts [12,15,19–21]; and in the case of propylene, it has been shown that including ceria in Pt and Pd catalysts reduces self-inhibition and decreases LO temperatures relative to Pd/Al_2O_3 catalysts under stoichiometric conditions [13,20,22].

While CO oxidation on PGM, PGM/Al_2O_3, PGM/Ceria catalysts has been well-studied, the kinetics and mechanism of hydrocarbon oxidation and simultaneous oxidation of CO and hydrocarbons under application-relevant conditions using model Pd/Al_2O_3 versus Pd/Ceria monolith catalysts have seen far fewer studies. Further insights into optimizing the oxidative component of Pd-based TWCs are thus desired from the perspective of more comprehensively understanding self- and mutual-inhibition of CO and HCs and reaction kinetics and mechanisms within nonisothermal monolith reactor systems. To this end, in this study, transient and steady-state reactor experiments using Pd monolith catalysts were conducted to more systematically interpret the role of support (CZO versus Al_2O_3) compositions on self-inhibition of individual species and co-inhibition during LO of CO and propylene (chosen as a model hydrocarbon). The key reactions studied and respective heats of reaction are:

$$CO + 0.5O_2 \rightarrow CO_2 \quad (\Delta H_r = -283\ kJ/mol\ CO) \quad (1)$$

$$C_3H_6 + 4.5O_2 \rightarrow 3CO_2 + 3H_2O \quad (\Delta H_r = -1926\ kJ/mol\ C_3H_6) \quad (2)$$

Reaction orders and activation energies of CO and propylene oxidation were determined and mechanistic reaction steps proposed. The results and postulated mechanisms provide insight into co-oxidation, inhibition, and optimization of catalyst composition and activity.

2. Experimental

2.1. Catalyst synthesis

2.1.1. Incipient wetness impregnation

The catalysts were synthesized by incipient wetness impregnation. Pd/CZO and Pd/Al_2O_3 catalysts were prepared with 1 wt% Pd in the washcoat and an overall washcoat loading of approximately 3 g/in^3 of monolith. Al_2O_3 (Sasol, 140 m^2/g) and CZO (Rhodia/Ford, 70 m^2/g) powders were calcined in air at 500 °C for 5 h prior to impregnation. Pd was deposited onto the support powders via an aqueous solution of Pd(II) nitrate hydrate (Alfa Aesar). The impregnated powder catalyst was dried at 120 °C for 20 h and then calcined in air at 500 °C for 5 h.

Table 1
Catalysts synthesized.

Fresh Catalyst	Pd/CZO	Pd/Al_2O_3
wt% Pd in washcoat	1.0	1.0
Pd loading (g/ft^3 of monolith)	55	52
Washcoat loading (g/in^3 of monolith)	3.2 g/in^3, CZO	3.0 g/in^3, Al_2O_3
BET Surface Area (m^2/g)	69.4	128
Pore width (Å)	326	157
Pore volume (cm^3/g)	0.565	0.504
Nanoparticle size (Å)	865	469
% Dispersion	11.4	23.3

2.1.2. Monolith washcoating

Blank 400 cpsi cordierite monolith samples (BASF-NGK) 0.5 in diameter and length were used. Synthesized catalyst powders were mixed in deionized water to create catalyst slurries. Dilute HNO_3 was added to reduce the slurry pH to approximately 3.5 for more effective ball milling and coating [23]. The catalyst slurries were ball-milled for 20 h. Monoliths were washcoated by alternately dipping ends of monoliths into slurries. To remove excess slurry in channels and achieve uniform coatings, air was blown through each end of the monolith after each dip-coating. Monoliths were then dried at 120 °C for 20 h. This procedure was repeated several times as necessary to reach the desired washcoat loading, after which the monoliths were calcined at 500 °C for 5 h. Catalyst properties including loadings, BET surface areas, pore properties, nanoparticle size, and percent Pd dispersion are provided in Table 1. Characterization was conducted using a Micromeritics ASAP 2020 instrument: physisorption (BET, pore properties, nanoparticle size) was carried out using N_2 gas at 77 K and chemisorption (percent Pd dispersion) using H_2 gas at 35 °C.

2.2. Reactor testing

2.2.1. Reactor system

The feed gas mixture was supplied by gas cylinders (Matheson Tri-Gas; Praxair, Inc.) and controlled using a series of mass flow controllers (MKS Inc.) Gas lines were wrapped with heating tape (heated to 130 °C) to prevent water condensation within the system. The reactor consisted of a cylindrical quartz tube placed inside a Lindbergh temperature controlled furnace. The monolith catalyst was placed inside the reactor tube. Four thermocouples (Omega) were placed inside the reactor system to monitor temperatures at four different axial positions: 20 cm upstream of the monolith, 1 cm before the front face of the monolith to monitor the feed (monolith entrance) gas temperature, halfway down the length of a central monolith channel to monitor the monolith temperature, and just inside the end of a monolith channel to measure the monolith end temperature. LabView™ software was used to control and record mass flow controller and thermocouple signals. The primary analytical system consisted of a FTIR spectrometer (MKS Inc., Multigas 2030) used to detect concentrations of CO, C_3H_6, and CO_2. MKS software was used to record FTIR signals.

2.2.2. Experimental conditions

Experiments were designed to simulate application-relevant space velocity (GHSV = 150,000 h^{-1}) with gas compositions comprising 0.1–1% CO, 250–500 ppm C_3H_6, O_2, and balance Ar. To study the differential kinetics of oxidation (i.e. estimate reaction orders and activation energies), CO or C_3H_6 conversion was held below 15%, with concentrations of one reactant varied while that of the other held constant. During LO experiments, O_2 concentrations were adjusted to give an air-fuel equivalence ratio λ of 1.01 (i.e.

a near-stoichiometric, slightly lean mixture). λ is defined as the ratio of the actual air-to-fuel ratio (AFR) to the stoichiometric AFR:

$$\lambda = \frac{AFR}{AFR_{stoich}} \quad (3)$$

Table 2 includes feed concentrations used in LO experiments. The feeds were devoid of H_2O and CO_2 for the current study. The lack of CO_2 is not expected to impact oxidation results. Though H_2O is noted to have an effect on CO and HC oxidation, it was excluded from feed mixtures to eliminate any complicating side reactions (e.g. water gas shift) and allow for focus on the fundamental performance and kinetics of oxidation reactions of interest.

Catalysts were pretreated in 10% O_2 (balance Ar) at 550 °C for 30 min before each set of experiments. For temperature programmed oxidation (TPO) experiments, the reactor furnace temperature was ramped at 3 °C/min from room temperature to 500 °C. Temperatures were held constant during steady-state experiments. The Pd/CZO catalyst was tested "fresh" (initial tests after synthesis) and after 10+ months of use ("deactivated").

3. Results

3.1. CO oxidation

3.1.1. CO oxidation kinetics

Steady-state kinetics experiments were conducted using the Pd/Al_2O_3 and Pd/CZO catalysts to estimate reaction orders and activation energies. Conventional ln(rate) versus $\ln(C_{ave})$ plots give an estimate of the CO reaction order for a prescribed temperature, where C_{ave} is the average of the reactant feed and effluent concentrations. Fig. 1a and b shows such data for CO oxidation on the three catalysts at different monolith temperatures (T). The reaction order with respect to CO is ~−1 for the Pd/Al_2O_3 catalyst and ~−0.52 to ~0.10 for the deactivated Pd/CZO catalyst. These observations are consistent with literature values for PGM/Al_2O_3 and PGM/CeO_2 catalysts, with negative reaction orders validating the self-inhibitory nature of CO and orders approaching zero demonstrating the promoting effects of ceria [7,15–18,24–26]. The error bounds shown in Fig. 1b lead to a range of CO reaction orders using Pd/CZO. Fig. 1c shows that the activation energy using the Pd/Al_2O_3 catalyst is in the range of 134–156 kJ/mol, consistent with literature values [15,25,26]. The observed activation energy decreases significantly to 25–70 kJ/mol using the Pd/CZO catalyst. The activation energy for the Pd/Al_2O_3 catalyst corresponds to the binding energy of CO on Pd [15,25,26], while the much lower value for the Pd/CZO catalyst suggests a change in reaction mechanism. We elaborate on the mechanism in the discussion section. Fig. 1d shows ln(rate) plotted versus $\ln(C_{in})$, where C_{in} is the inlet feed concentration of O_2. The reaction order with respect to O_2 using the Pd/Al_2O_3 catalyst is approximately 1, as reported in the literature for PGM/Al_2O_3 catalysts [15,17,25–27]. Using the Pd/CZO catalyst, the observed reaction order with respect to O_2 is slightly positive (approximately 0.3); fractional orders (0–0.6) have been reported in the literature for PGM/CeO_2 and $PGM/CeO_2/Al_2O_3$ catalysts [11,15,17,18].

3.1.2. CO light-off behavior

Conversion versus monolith temperature results for CO TPO experiments are shown in Fig. 2. LO curves were generated as the reactor was ramped up in temperature while gas mixtures containing 0.5% or 1% CO were fed to the reactor. Using both Pd/Al_2O_3 and Pd/CZO catalysts, the temperature spanned a sufficiently wide range to include negligible conversion and nearly complete conversion. The Pd/CZO catalyst results are shown when the catalyst was tested fresh and deactivated. The data indicate that complete conversion of CO is achieved with the required temperature dependent on the catalyst composition and CO concentration. With increasing CO feed concentration of CO, the LO curves shift to the right. The higher temperatures required to light-off the higher feed concentrations of CO demonstrate that CO is a self-inhibiting species. For example, using the Pd/Al_2O_3 catalyst, the monolith temperature at which 50% conversion of CO is achieved (T50) increases from 216 °C with a feed concentration of 0.5% CO to 225 °C with 1% CO. Additional T50 temperatures are provided in Table 3. The apparent benefit of ceria is evident given that CO light off occurs at lower temperatures using Pd/CZO, even as the Pd/CZO catalyst experiences a loss in activity with use over time. As listed in Table 3, T10 (monolith temperature at which 10% CO conversion is achieved) and T50 values decrease using the Pd/CZO catalyst. Examining oxidation of 1% CO, T50 values are 225 °C with Pd/Al_2O_3, 164 °C with fresh Pd/CZO, and 195 °C with deactivated Pd/CZO. The CO oxidation rate is clearly enhanced with Pd/CZO compared to Pd/Al_2O_3.

The activity of the deactivated Pd/CZO catalyst was further studied during steady-state CO oxidation experiments with feed concentrations of 0.5% CO, 0.6% CO, and 1% CO (λ = 1.01 in all experiments). Steady-state conversion versus monolith temperature data are shown in Fig. 3. T10 and T50 temperatures increase with increasing CO concentration, demonstrating the self-inhibiting nature of CO under steady-state conditions as observed during transient temperature ramp experiments. Under differential, low conversion conditions, experimental error contributes to less clarity in the dependence of CO conversion and CO feed concentration. We explored this in the previous section on CO oxidation kinetics.

In Fig. 4, monolith temperatures corresponding to Pd/CZO and Pd/Al_2O_3 LO data in Fig. 1 are plotted versus gas feed temperature, which was recorded at the entrance of the monolith. CO oxidation is exothermic and the amount of heat released and thus the temperature rise is dependent on CO concentration. A temperature rise is noted, the magnitude of which is the difference between the monolith temperature and feed temperature. As expected, the temperature rise commences at lower feed temperatures using the more active Pd/CZO catalyst for both studied feed concentrations of 0.5% and 1% CO. For both Pd/CZO and Pd/Al_2O_3 the maximum difference between monolith and feed temperatures during oxidation of 0.5% CO is approximately 65 °C (feed temperature: 178 °C), about half of the roughly 120 °C rise observed during 1% CO oxidation (feed temperature: 156 °C). As the feed temperature increases, the difference between monolith and feed temperatures diminishes slightly. For instance, using Pd/CZO to oxidize 1% CO, for a feed temperature of approximately 360 °C, the monolith temperature is 85 °C higher. A comparison of the observed experimental temperature rise with theoretical adiabatic temperature rise is detailed in the discussion section.

3.2. Propylene oxidation

3.2.1. Propylene oxidation kinetics

The steady-state propylene oxidation rate versus average concentration data are plotted in Fig. 5a. The reaction order with respect to propylene is in the range of −0.78 to −0.75 for both Pd/Al_2O_3 and Pd/CZO catalysts. The negative-order is an expected outcome for Pd without ceria as propylene is a self-inhibiting species, with values comparable to literature values [15,28,29]. Arrhenius plots shown in Fig. 5b reveal propylene oxidation activation energies of 72–105 kJ/mol using both catalysts, approximately half of that observed for CO oxidation and similar to literature values [15,28]. Fig. 5c shows ln(rate) plotted versus $\ln(C_{in})$, where C_{in} is the inlet feed concentration of O_2; reaction orders with respect to O_2 using both catalysts are extrapolated from the fitted data. The reaction order with respect to O_2 is in the range of 1.17–1.79 using the Pd/Al_2O_3 catalyst and 1.38–1.45 using the Pd/CZO catalyst, within range of literature values (0.2–1.5) for Pd based catalysts (Pd wire, Pd/SiO_2, Pd/Al_2O_3, $Pd/CeO_2/Al_2O_3$) [15,28,29]. Table 4

Table 2
LO experiment feed concentrations.

Feed Gas	CO LO		C_3H_6 LO		Mixture LO
CO (%)	0.5	1.0			1.0
C_3H_6 (ppm)			250	500	500
O_2 (%)	0.45	0.70	0.31	0.42	0.89

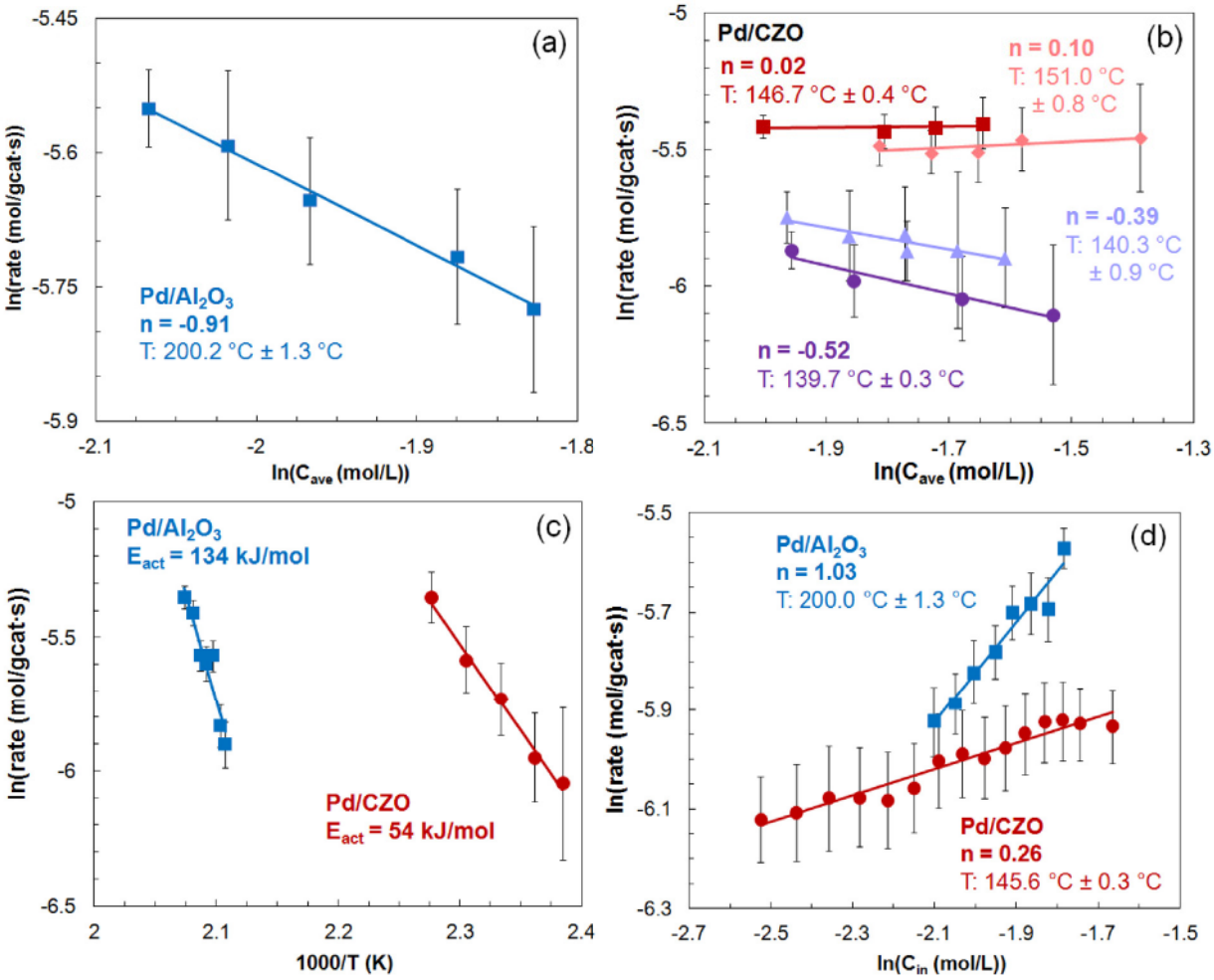

Fig. 1. (a) Reaction order with respect to CO on Pd/Al_2O_3 (b) Reaction order with respect to CO on deactivated Pd/CZO (c) Activation energies of CO oxidation (0.6% CO) (d) Reaction orders with respect to O_2. Vertical error bars and margin of error represent standard deviation from the mean.

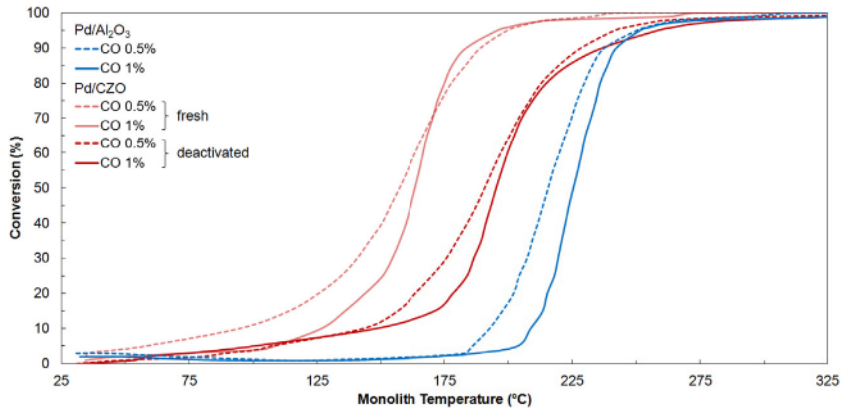

Fig. 2. CO LO on Pd/Al_2O_3 and Pd/CZO. Conditions: 0.5% or 1% CO, O_2 for $\lambda = 1.01$, balance Ar, GHSV = 150,000 h^{-1}, temperature ramp 3 °C/min.

Table 3
LO temperatures for CO oxidation.

Catalyst	Pd/Al_2O_3		Pd/CZO (fresh, deactivated)	
CO feed	0.5%	1%	0.5%	1%
T10 (°C)	193	209	95, 141	127, 148
T50 (°C)	216	225	157, 191	164, 195
Maximum conversion	100	100	100, 100	100, 100

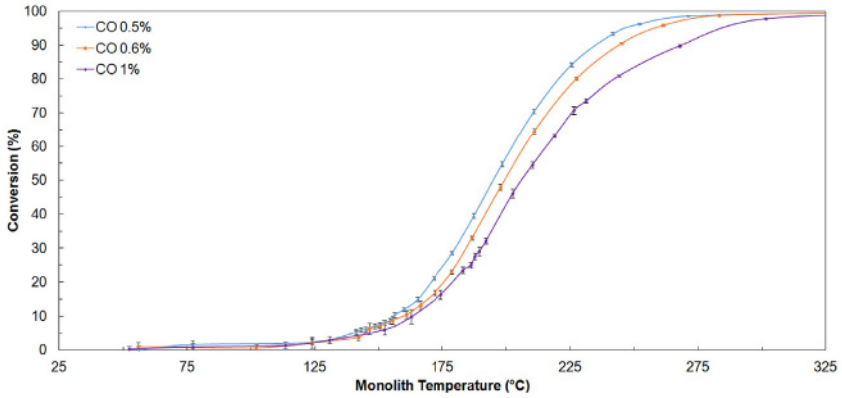

Fig. 3. Steady-state CO oxidation on deactivated Pd/CZO. Conditions: 0.5%, 0.6%, or 1% CO, O_2 for $\lambda = 1.01$, balance Ar, GHSV = 150,000 h^{-1}. Vertical error bars represent standard error of the mean CO conversion.

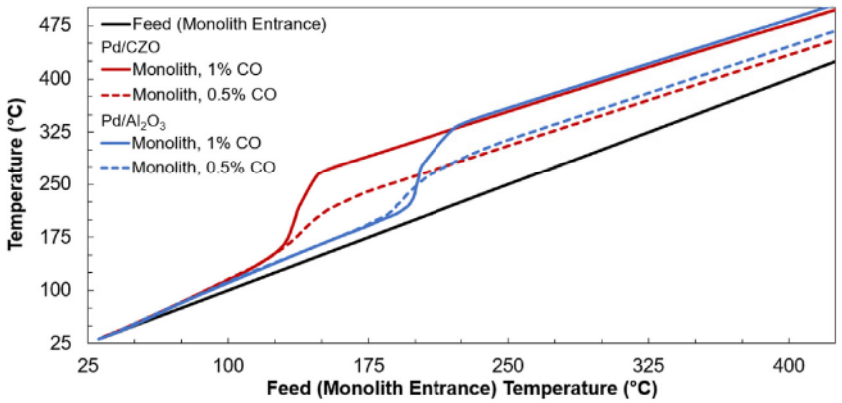

Fig. 4. Temperature rise during CO LO. Conditions: 0.5% or 1% CO, O_2 for $\lambda = 1.01$, balance Ar, GHSV = 150,000 h^{-1}, temperature ramp 3 °C/min.

Table 4
Kinetic parameters for CO, C_3H_6 oxidation.

Catalyst	CO Reaction Order	CO E_{act} (kJ/mol)	C_3H_6 Reaction Order	C_3H_6 E_{act} (kJ/mol)	O_2 Reaction Order for CO oxidation	O_2 Reaction Order for C_3H_6 oxidation
Pd/Al_2O_3	−0.91	134–156	−0.78	72–105	1.02–1.03	1.17–1.79
Pd/CZO	−0.52 to 0.10	25–70	−0.75	88–95	0.26–0.29	1.38–1.45

lists ranges of reaction orders and activation energies for additional data collected. Later we speculate on the nature of observed reaction orders and why C_3H_6 self-inhibition is not mitigated at low temperatures using ceria.

3.2.2. *Propylene light-off behavior*

LO experiments similar to CO were carried out for propylene. Fig. 6 shows the LO behavior of propylene using feed concentrations of 250 ppm and 500 ppm. For both catalysts, increasing the feed concentration of propylene shifts the LO curves to higher temperatures. Thus, like CO, propylene is a self-inhibiting species. Whereas CO was completely converted under the experimental conditions, propylene was not, even at temperatures as high as 500 °C. As listed in Table 5, the asymptotic limit of the propylene conversion is in the range of 93–94% using Pd/Al_2O_3 and 98% using Pd/CZO. We expand on these limits and related mass transport effects in the discussion section. At lower temperatures (<200 °C), propylene conversion is not enhanced with the addition of ceria to the extent that it is during CO oxidation. The T10 temperatures are fairly similar using both catalysts: roughly 170 °C for a feed concentration of 250 ppm C_3H_6 and 190 °C for 500 ppm C_3H_6. Another difference in comparison to CO oxidation is that over a range of intermediate temperatures (200–300 °C), a lag in conversion or "shoulder" is observed for the LO curves using the Pd/Al_2O_3 catalyst. This unconventional LO curve feature (i.e., for a single overall catalytic reaction) does not appear during propylene LO using Pd/CZO. As a result of the lag in conversion, T50 temperatures differ using the two catalysts: for a feed concentration of 500 ppm C_3H_6, T50 values are 226 °C using

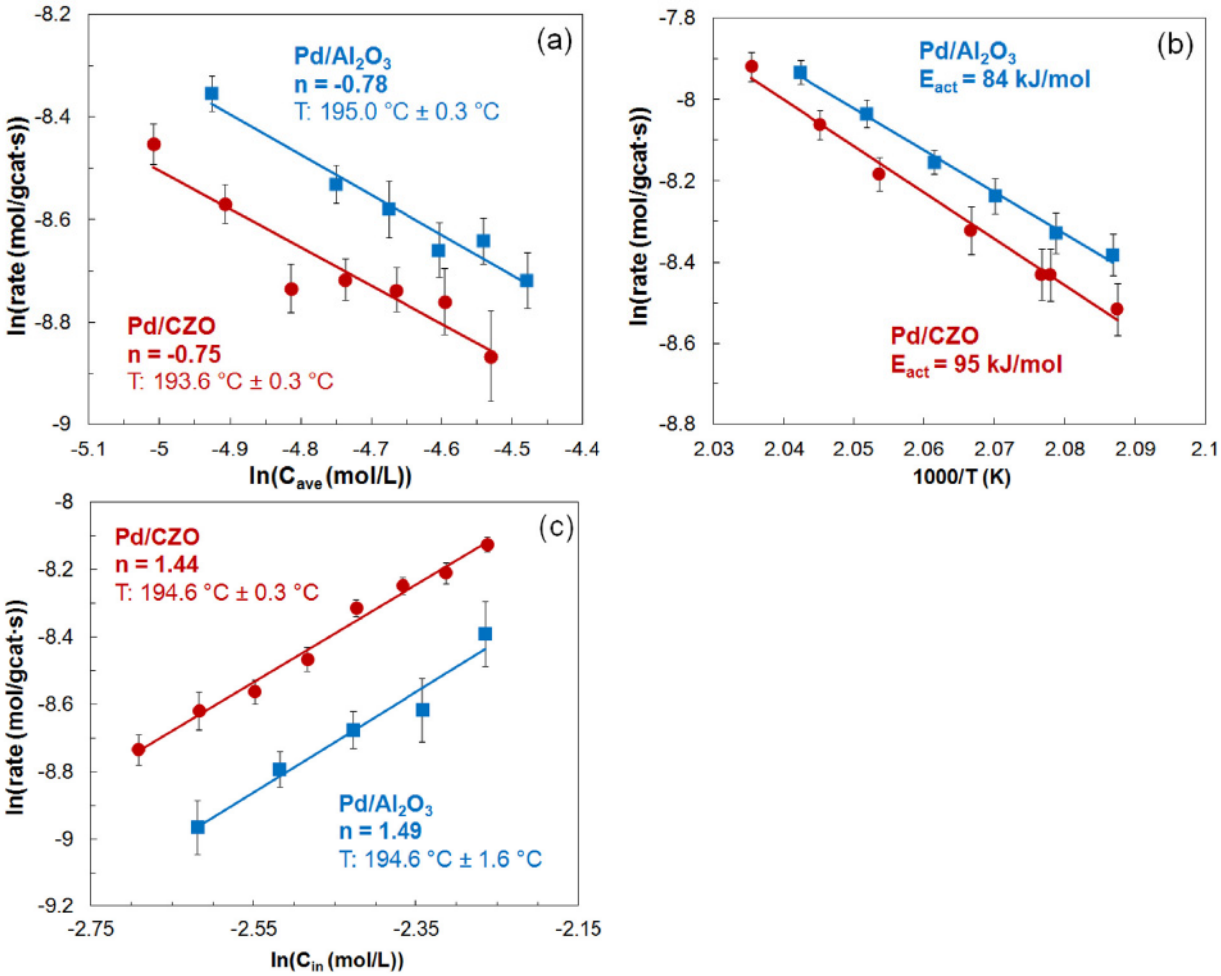

Fig. 5. (a) Reaction orders with respect to C_3H_6 at 193–195 °C (b) Activation energies of C_3H_6 oxidation using 500 ppm C_3H_6 (c) Reaction orders with respect to O_2 at 195–199 °C. Vertical error bars and margin of error represent standard deviation from the mean.

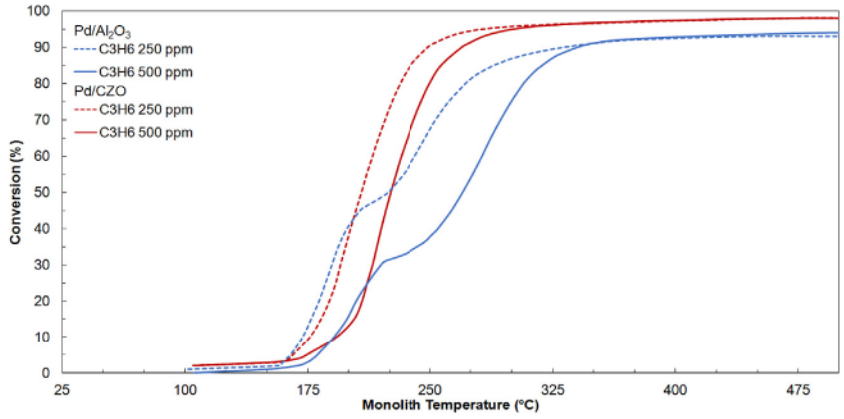

Fig. 6. C_3H_6 LO on Pd/Al_2O_3 and Pd/CZO. Conditions: 250 ppm or 500 ppm C_3H_6, O_2 for $\lambda = 1.01$, balance Ar, GHSV = 150,000 h^{-1}, temperature ramp 3 °C/min.

Table 5
LO temperatures for propylene oxidation.

Catalyst	Pd/Al_2O_3		Pd/CZO	
C_3H_6 feed	250 ppm	500 ppm	250 ppm	500 ppm
T10 (°C)	172	191	176	193
T50 (°C)	224	270	208	226
Maximum conversion	93	94	98	98

Pd/CZO and 276 °C using Pd/Al_2O_3. This trend may be interpreted as rate enhancement by ceria for propylene oxidation. We return to this point later.

3.2.3. Propylene temperature ramp cycling vs. steady-state oxidation

Using both Pd/Al_2O_3 and Pd/CZO catalysts, additional temperature ramp cycling and steady-state oxidation experiments were conducted using 500 ppm C_3H_6 in the feed ($\lambda = 1.01$). The intent was to obtain some additional information about the conversion shoulder and lack thereof observed using the Pd/Al_2O_3 and Pd/CZO catalysts, respectively. Fig. 7 compares propylene conversion during steady-state oxidation and cycling experiments (during which the reactor is ramped up in temperature, then down, and up a second time) using (a) Pd/Al_2O_3 and (b) Pd/CZO. Using both catalysts, with cycled temperature ramps, the oxidation temperatures shift higher, demonstrating a clockwise hysteresis trend.

Using the Pd/Al_2O_3 catalyst, the shoulder is diminished with cycling. Furthermore, waiting even longer times to capture the actual steady-state (time invariant) oxidation trends, the conversion at any given monolith temperature is even lower and no shoulder at intermediate temperatures is apparent. T10 increases from 183 °C during the first ramp-up to 201 °C during both the ramp-down and second ramp-up to 216 °C during steady-state oxidation. T50 is 233 °C during the first ramp-up, 245 °C during the ramp-down, 238 °C during the second ramp-up, and 260 °C at steady-state.

The LO results for Pd/CZO show both similar and dissimilar features. As for Pd/Al_2O_3, T10 temperatures increase over the course of cycling using the Pd/CZO catalyst; from 189 °C during the first ramp-up to 205 °C during the ramp-down. However, T10 then shifts lower to 199 °C during the second ramp-up and 203 °C during steady-state oxidation. T50 shows a comparable trend; it increases from 223 °C during the first ramp-up to 238 °C during the ramp-down. During the second ramp-up, T50 is 224 °C, i.e. the LO curve is similar to that of the first ramp-up above ~50% conversion. T50 during steady-state experiments is 233 °C – lower than that of the second ramp-up. In fact, the propylene conversion during steady-state oxidation is higher than that during the temperature ramp-down – contrary to what was observed using the Pd/Al_2O_3 catalyst. The conversion is lower during the ramp-down than the ramp-up's, demonstrating clockwise hysteresis effects. While oxidation is inhibited at lower temperatures during the second ramp-up (suggesting inhibition due to carbonaceous species accumulating over the course of the cycling experiment), conversion matches that of the initial ramp-up. Ceria-supplied oxygen could play a greater role at intermediate and high temperatures over the course of the temperature ramp-up. During steady-state oxidation, the conversion is in fact higher than that during the temperature ramp-down. Allowing the catalyst to operate under the same conditions over relatively longer periods of time could lead to enhancement of re-oxidation of ceria and oxidation by ceria greater than that during the transient cooling down segment of the cycling experiment. Mechanistic reaction steps are proposed in the discussion section to speculate the cause of these trends.

3.3. CO + C_3H_6 co-oxidation: light-off behavior

3.3.1. Individual vs. co-oxidation

The co-oxidation behavior was examined by co-feeding CO and propylene. In Fig. 8a, individual oxidation LO curves for 1% CO and 500 ppm propylene are compared to curves generated during co-oxidation of a feed mixture of 1% CO and 500 ppm propylene using Pd/Al_2O_3. When CO and propylene are mixed and co-fed at the indicated concentrations, ignition is delayed to higher temperatures. As listed in Table 6, T50 shifts from 225 °C when 1% CO is oxidized alone to 266 °C when 1% CO is oxidized in the presence of 500 ppm of propylene, demonstrating that propylene inhibits CO oxidation. While T50 for propylene oxidation does not shift significantly from the individual oxidation to co-oxidation, T10 increases from 191 °C to 249 °C, illustrating the inhibiting effect CO has on propylene oxidation. Thus, CO and propylene are mutually inhibiting. Comparing T10 temperatures of all four LO curves in Fig. 8a, a change in order of LO is observed under these experimental conditions: 500 ppm propylene begins oxidizing at a lower temperature (191 °C) than 1% CO (209 °C) during individual oxidation, but during co-oxidation T10 for CO is 244 °C and 249 °C for propylene. An additional point of interest is the lack of a shoulder in conversion in the propylene LO curve during co-oxidation.

Fig. 8b compares the analogous set of LO curves generated using the Pd/CZO catalyst. Under the same experimental conditions, CO and propylene are similarly mutually inhibiting using the Pd/CZO catalyst. For CO oxidation, T10 increases by 53 °C and T50 increases by 65 °C in the presence of 500 ppm propylene. Propylene oxidation LO temperatures are also listed in Table 6; both T10 and T50 temperatures increase in the presence of CO. Unlike oxidation order trends observed using Pd/Al_2O_3, CO lights off before propylene during both individual oxidation and co-oxidation using Pd/CZO, and no shoulder in LO curves is observed.

3.3.2. Co-oxidation compared using both catalysts

Comparing the co-oxidation behavior of CO and propylene using both catalysts, Fig. 9 reiterates the observation that CO lights off before propylene under the experimental conditions studied. The lowest LO temperatures are achieved using the Pd/CZO catalyst. Another benefit of using CZO in the catalyst appears to have a sharper, more efficient ignition leading to higher conversion limits reached at lower temperatures relative to co-oxidation on Pd/Al_2O_3.

4. Discussion

4.1. CO oxidation mechanisms

Pd-catalyzed CO oxidation is a well-studied reaction system, with many studies focused on the mechanism and/or kinetics [7,25,26,30–35]. Even more studies have appeared on the related Pt-catalyzed CO oxidation. Reaction mechanisms of CO oxidation using Pd on the two different support materials, Al_2O_3 and CZO, are depicted schematically in Fig. 10 [36].

Pd/Al_2O_3 catalyzed CO oxidation is generally considered to follow the four-step sequence:

$$CO + X \rightleftharpoons CO \cdot X \quad (R1)$$

$$O_2 + X \rightleftharpoons O_2 \cdot X \quad (R2)$$

$$O_2 \cdot X + X \rightleftharpoons 2O \cdot X \quad (R3)$$

$$CO \cdot X + O \cdot X \rightarrow CO_2 + 2X \quad (R4)$$

where X denotes a single Pd site. Sometimes the mechanistic sequence is shown as three steps with steps R2 and R3 combined as follows:

$$O_2 + 2X \rightleftharpoons 2O \cdot X \quad (R5)$$

Note that while (R5) is second order with respect to the vacant sites, the reaction is considered first-order in the vacant sites.

For temperatures below the LO temperature, CO adsorbs onto Pd active sites (X) dispersed on both support materials, preventing O_2 from competitively adsorbing and dissociating. On Pd/Al_2O_3, the overall reaction is limited by CO desorption – as the temperature increases, CO desorption occurs and reaction proceeds readily. In

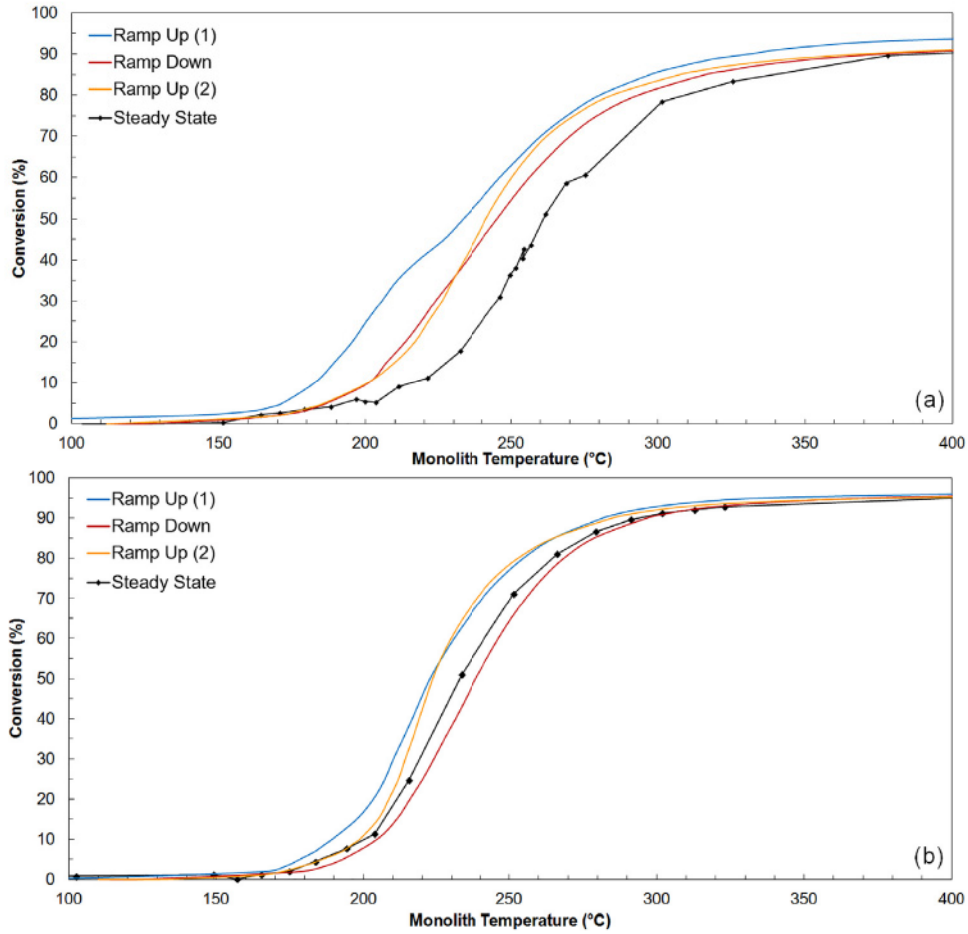

Fig. 7. C_3H_6 cycling and steady-state oxidation on (a) Pd/Al_2O_3 and (b) Pd/CZO. Conditions: 500 ppm C_3H_6, 4200 ppm O_2 ($\lambda = 1.01$), balance Ar, GHSV = 150,000 h^{-1}, temperature ramp 3 °C/min.

Table 6
Light-off temperatures, asymptotic limits for CO, C_3H_6 oxidation.

Catalyst	Pd/Al_2O_3			Pd/CZO		
Feed	CO 1%	C_3H_6 500 ppm	CO 1% + C_3H_6 500 ppm (CO, C_3H_6)	CO 1%	C_3H_6 500 ppm	CO 1% + C_3H_6 500 ppm (CO, C_3H_6)
T10 (°C)	209	191	244, 249	127	193	180, 207
T50 (°C)	225	270	266, 272	164	226	229, 232
Maximum conversion	100	94	99, 97	100	98	100, 99

the limit of a CO covered surface ($\theta_{CO} \to 1$, where θ_{CO} is the surface coverage of CO) and assuming O_2 adsorption and dissociation (R5) to be first order with respect to O_2 concentration, the rate expression for CO_2 production is easily derived and is as follows [33,37]:

$$Rate = A_{d,CO} \exp\left(-\frac{E_{d,CO}}{RT}\right) \frac{k_{a,O_2} p_{O_2}}{k_{a,CO} p_{CO}} \quad (4)$$

where $A_{d,CO}$ ($E_{d,CO}$) is the pre-exponential factor (activation energy) for CO desorption, $k_{a,O2}$ and $k_{a,CO}$ are the respective adsorption rate constants for O_2 and CO, and p_{O2} and p_{CO} are the respective partial pressures of O_2 and CO. The reaction order is −1 (+1) with respect to CO (O_2) with the apparent activation energy equal to CO binding energy to Pd.

For CO oxidation using Pd/CZO, an additional set of steps involving ceria may occur as follows:

$$O_2 + 2Y \to 2O \cdot Y \quad (R6)$$

$$O \cdot X + Y \rightleftharpoons O \cdot Y + X \quad (R7)$$

$$CO \cdot X + O \cdot Y \to CO_2 + X + Y \quad (R8)$$

where Y denotes an oxygen storage site on ceria, which is generally considered an oxygen vacancy. Uptake of oxygen occurs directly from the gas phase (R6) or via spillover of oxygen initially adsorbed on Pd (R7). When ceria has a sufficiently high loading, the surface reaction between adsorbed CO and O (R4) is augmented by an interfacial reaction involving adsorbed CO and O supplied by ceria (R8).

Focusing on the case of a CO covered Pd surface, the steady-state coverages balances for CO, O, and O-Y are derived considering (R1), (R4)–(R6), and R(8):

$$k_{a,CO} p_{CO} \theta_v - k_{d,CO} \theta_{CO} - k_r \theta_{CO} \theta_O - k_{rY} \theta_{CO} \theta_{OY} = 0 \quad (5)$$

$$2k_{a,O_2} p_{O_2} \theta_v - k_r \theta_{CO} \theta_O = 0 \quad (6)$$

$$2k_{a,O_2} p_{O_2} \theta_{vY} - k_{rY} \theta_{CO} \theta_{OY} = 0 \quad (7)$$

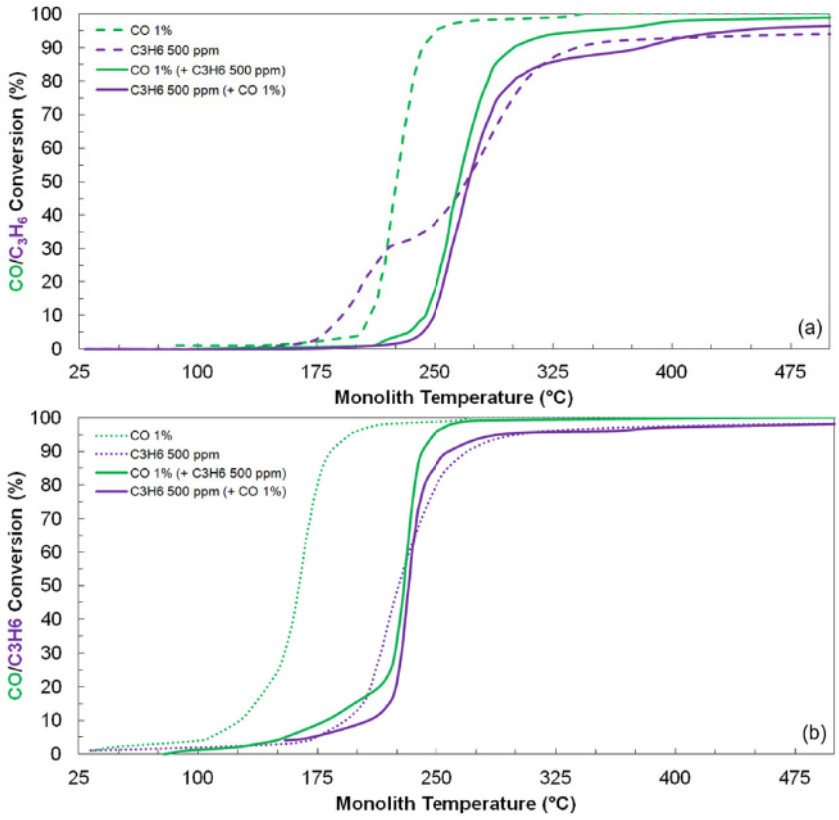

Fig. 8. 1% CO, 500 ppm C_3H_6, and 1% CO + 500 ppm C_3H_6 LO on (a) Pd/Al_2O_3 (b) Pd/CZO. Conditions: O_2 for $\lambda = 1.01$, balance Ar, GHSV = 150,000 h^{-1}, temperature ramp 3 °C/min.

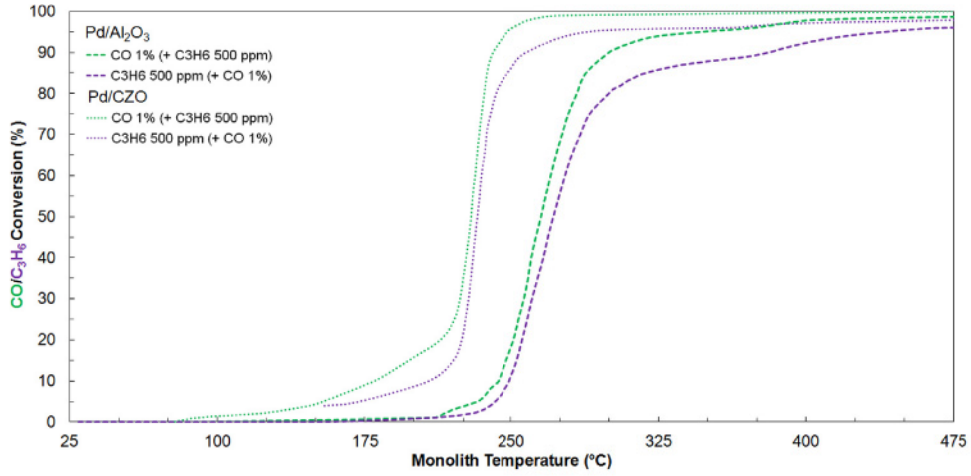

Fig. 9. Co-oxidation of 1% CO and 500 ppm C_3H_6 on Pd/Al_2O_3 and Pd/CZO. Conditions: 0.89% O_2 ($\lambda = 1.01$), balance Ar, GHSV = 150,000 h^{-1}, temperature ramp 3 °C/min.

where θ_i is the surface coverage of species i, k_r is the rate constant for (R5) and k_{rY} is the rate constant for (R8). The rate of CO_2 production thus includes contributions from both (R5) and (R8):

$$Rate = k_r\theta_{CO}\theta_O + k_{rY}\theta_{CO}\theta_{OY} \quad (8)$$

If we assume that Pd surface and ceria oxygen storage site vacancies are balanced by coverages of CO (Eq. (9)) and O-Y (Eq. (10)), respectively, the coverage of O-Y can be derived to be dependent on the coverage of CO (Eq. (11)):

$$\theta_v \approx 1 - \theta_{CO} \quad (9)$$

$$\theta_{vY} = 1 - \theta_{OY} \quad (10)$$

$$\theta_{OY} = \frac{2k_{a,O_2}p_{O_2}}{2k_{a,O_2}p_{O_2} + k_{rY}\theta_{CO}} \quad (11)$$

Thus, utilizing (Eq. (11)) and coverage balances (Eqs. (5)–(7)), a quadratic expression involving θ_{CO} is obtained:

$$a\theta_{CO}^2 + b\theta_{CO} + c = 0 \quad (12)$$

$$a = k_{rY}\left(k_{a,CO}p_{CO} + k_{d,CO} - 2k_{a,O_2}p_{O_2}\right) \quad (13)$$

$$b = 2k_{a,O_2}p_{O_2}\left(k_{a,CO}p_{CO} + k_{d,CO} - 2k_{a,O_2}p_{O_2}\right) + k_{rY}\left(k_{a,CO}p_{CO} - 4k_{a,O_2}p_{O_2}\right) \quad (14)$$

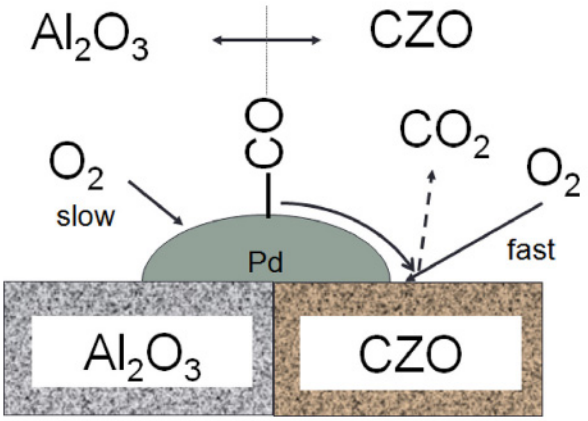

Fig. 10. CO oxidation on Pd/Al_2O_3 vs Pd/CZO. Adapted from Cheng and McCabe [36].

$$c = 2k_{a,O_2}p_{O_2}\left(k_{a,CO}p_{CO} - 2k_{a,O_2}p_{O_2}\right) \quad (15)$$

θ_{CO} can be solved for and used to calculate θ_O and θ_{OY}, as required to estimate the overall rate of CO_2 production (Eq. (8)). In the limiting case when $k_{rY} = 0$ (i.e. ceria is not involved and CO oxidation proceeds on Pd), the overall rate expression collapses to that derived in Eq. (4). For large k_{rY} (i.e. ceria plays a significant role in CO oxidation), the coverage analysis can be shown to predict a reaction order of zero with respect to CO, as observed in experiments using Pd/CZO. This alternate reaction mechanism could provide a lower energy barrier for CO oxidation, as observed when estimating the activation energy using the Pd/CZO catalyst.

Another model for interpreting CO oxidation with oxygen supplied by ceria involves reactions (R1) and (R6)–(R8) via a Mars Van Krevelen-type mechanism, where at steady state, the rate of reaction can be derived using the rate of CO oxidation (assuming first order with respect to CO) and rate of ceria re-oxidation (assumed to be proportional to the partial pressure of O_2 and concentration of active sites not covered by oxygen):

$$Rate = \left[\frac{1}{k_{rY}\theta_{CO,I}} + \frac{1}{k_Y p_{O_2}^{1/2}}\right]^{-1} \cong k_Y p_{O_2}^{1/2} \ldots\ldots\ldots with\ k_{rY}\theta_{CO,I} \gg k_Y p_{O_2}^{1/2} \quad (16)$$

$$\theta_{CO,I} = \frac{K_{CO}p_{CO}}{1 + K_{CO}p_{CO}} \quad (17)$$

$$K_{CO} = \frac{k_{a,CO}}{k_{d,CO}} \quad (18)$$

where k_{rY} is the rate constant for reaction between adsorbed CO and O supplied by ceria (R8); $\theta_{CO,I}$, the surface coverage of CO; k_Y is the rate constant of the uptake of bulk oxygen by ceria vacancies (R6). As shown in the rate expression in Eq. (16), the overall rate is zero order with respect to CO and half order with respect to O_2. Using the Pd/CZO catalyst, differential kinetic experiments demonstrated a reaction order of zero with respect to CO and approximately 0.3 with respect to O_2, corroborating the rate expression analysis in the limiting case of CO oxidation using oxygen supplied by ceria.

A key assumption made thus far is that the rate of CO oxidation is independent of metal-particle size. This has been shown to be the case for CO oxidation on Pd/Al_2O_3; however, the rate of CO oxidation on Pd/Ceria has been observed to increase with decreasing Pd nanocrystal size [11]. That is, the effective length of the Pd/Ceria interface is a key determinant in the rate of CO oxidation [11]. We analyze the role of Pd particle size (length of the Pd/Ceria interface) in addition to mechanisms detailed and rate expressions derived for CO oxidation on Pd active sites and involving ceria-supplied oxygen in greater detail elsewhere [42].

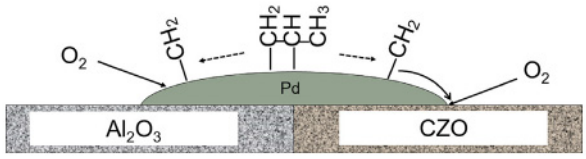

Fig. 11. C_3H_6 adsorption, fragmentation, and oxidation on Pd/Al_2O_3 vs Pd/CZO.

4.2. Propylene oxidation mechanism

For propylene oxidation on Pd catalysts, multiple steps involving various partial oxidation products can be considered. A mechanistic sequence for propylene involving methylene and CO surface species is proposed as follows:

$$C_3H_6 + X \rightleftharpoons C_3H_6 \cdot X \quad (R9)$$

$$O_2 + 2X \rightleftharpoons 2O \cdot X \quad (R5)$$

$$C_3H_6 \cdot X + 9O \cdot X \rightarrow 3CO_2 + 3H_2O + 10X \quad (R10)$$

$$C_3H_6 \cdot X + 2X \rightarrow 3CH_2 \quad (R11)$$

$$CH_2 \cdot X + 3O \cdot X \rightarrow CO_2 + H_2O + 4X \quad (R12)$$

$$CH_2 \cdot X + O \cdot X + X \rightarrow CO \cdot X + 2H \cdot X \quad (R13)$$

$$CO \cdot X + O \cdot X \rightarrow CO_2 + 2X \quad (R4)$$

$$2H \cdot X + O \cdot X \rightarrow H_2O + 3X \quad (R14)$$

Fig. 11 provides a schematic of the main features of the model.

At low temperatures, propylene adsorbs onto Pd active sites (R9), inhibiting the competitive adsorption and dissociation of oxygen (R5). As a result, (R10) involving the reaction of adsorbed propylene and adsorbed oxygen will not readily occur. It could also be that the energy barrier for this reaction is too high for this reaction to be dominant over a wide range of temperatures. At intermediate temperatures, propylene dissociates into smaller CH_2 fragments (R11), which can be oxidized into adsorbed CO and H (R13). Work by Hazlett et al. using bimetallic Pt-Pd/Al_2O_3 powder catalysts for propylene oxidation in excess O_2 showed that ethylene and CO byproducts may accumulate and deactivate the catalysts [38]. Considering alternate alkenes, a study by Steininger et al. using a Pt single crystal catalyst showed that ethylene undergoes dehydrogenation with increasing temperature, and decomposes in the presence of oxygen to form hydrogen and water (eventually undergoing combustion) [39]. As such, extrapolating this type of hydrocarbon decomposition behavior to propylene on Pd, multiple species may accumulate and inhibit oxidation, leading to a lag in conversion as observed during LO experiments using the Pd/Al_2O_3 catalyst. These species can then be oxidized at higher temperatures ((R12), (R4), and (R14)). During transient cycling experiments, carbonaceous species could further accumulate on the catalyst over the course of the experiment and lower the overall observed conversion of propylene (i.e., as seen in Fig. 7). Waiting even longer times to capture steady-state oxidation trends, increased amounts of carbonaceous species could further inhibit oxidation, such that the conversion at any given monolith temperature is even lower (e.g. using Pd/Al_2O_3, as seen in Fig. 7a).

Analogous reaction steps involving propylene oxidation via ceria are as follows:

$$O_2 + 2Y \rightleftharpoons 2O \cdot Y \quad (R6)$$

$$C_3H_6 \cdot X + 9O \cdot Y \rightarrow 3CO_2 + 3H_2O + X + 9Y \quad (R15)$$

$$CH_2 \cdot X + 3O \cdot Y \rightarrow CO_2 + H_2O + X + 3Y \quad (R16)$$

$$CH_2 \cdot X + O \cdot Y + 2X \rightarrow CO \cdot X + 2H \cdot X + Y \quad (R17)$$

$$CO \cdot X + O \cdot Y \rightarrow CO_2 + X + Y \quad (R8)$$

$$2H \cdot X + O \cdot Y \rightarrow H_2O + 2X + Y \quad \text{(R18)}$$

Whereas the CO oxidation rate is enhanced at low temperatures with the use of ceria, the experiments did not convey similar enhancement for propylene oxidation. This suggests that the reaction between adsorbed propylene and oxygen supplied by ceria does not occur readily. Or it could occur at a similar rate as the reaction between adsorbed propylene and adsorbed oxygen, or have a similarly high energy barrier at low temperatures.

At higher temperatures, propylene conversion exhibited enhancement using the Pd/CZO catalyst. This suggests that oxygen supplied by ceria contributes to reactions involving the oxidation of smaller adsorbed species like CH_2, CO, and H to the extent that a lag in conversion or shoulder in the LO curve does not appear.

When studying propylene oxidation at lower temperatures under differential conditions, the reaction order with respect to O_2 was observed to be greater than 1 using both Pd/Al_2O_3 and Pd/CZO catalysts. The oxidation kinetics and proposed mechanisms will be further explored in forthcoming modeling studies [42].

4.2.1. Asymptotic limit in conversion: transverse Peclet number analysis

The experiments demonstrate that CO and propylene are oxidized to different asymptotic conversion limits under the experimental conditions utilized. For example, as listed in Table 6, 1% CO is completely oxidized (100% conversion) whereas 500 ppm of C_3H_6 achieves 94% conversion using Pd/Al_2O_3 and 98% using Pd/CZO. The differences between the asymptotic conversions of CO versus propylene could be attributed to mass transfer limitations under the given experimental conditions. The relevant dimensionless groups are as follows:

$$P = \frac{R_\Omega^2 < u >}{LD_m} \quad (19)$$

$$Pe = \frac{< u > L}{D_m} \quad (20)$$

$$Sc = \frac{\nu}{D_m} \quad (21)$$

where <u> is the average velocity in the monolith channel, D_m is the molecular diffusivity of the reactant species, R_Ω is the ratio of channel cross-sectional area to perimeter, L is the channel length, and ν is the kinematic viscosity. A transverse Peclet (P) number analysis shows that the differences in species diffusivities lead to different conversions at the exit of a monolith channel, depending on Schmidt (Sc) and axial Peclet (Pe) numbers [40]. P is the ratio of the species transverse diffusion time to convection time; the smaller is P, the faster is the rate of transverse diffusion of species to the channel walls where reactions occur, the higher is the overall exit conversion. This analysis ignores any diffusion limitations within the washcoat.

Table 7 lists the estimated transverse and axial Peclet numbers for CO and C_3H_6 for feed temperatures of 300 °C to 600 °C and feed concentrations of 1% CO or 500 ppm C_3H_6. The parameter values are based on the reactor system used in experiments and from the literature [41]. Diffusivities (D) for CO and C_3H_6 are also noted in Table 7, where coefficient values increase with increasing temperatures. Assuming a large Schmidt number (flow in the monolith channel more closely resembles a fully developed velocity profile rather than flat velocity profile), the theoretical exit conversion lies between the limit when the axial Peclet number equals zero (short monolith model) and the limit when the axial Peclet number is infinite (convection model with 100% conversion) [40]. Lower bounds in conversion exist when Pe is estimated to be zero. For example, for $Sc \rightarrow \infty$, Pe = 0, and P = 0.10, the expected exit conversion is 91.7% [40]. For the same Sc and Pe but P = 0.25, the exit conversion is 81.9% [40]. The calculated Pe values at 300 °C, 400 °C, 500 °C, and 600 °C are listed in Table 7. As the numbers are relatively large, the theoretical conversion could be expected to be closer to the upper bound derived for $Pe \rightarrow \infty$. For the range of temperatures tabulated, P for CO is estimated to be between 0.10 and 0.05, such that the expected upper bound on conversion is 100%. P for C_3H_6 is calculated to decrease from 0.17 at a temperature of 300 °C to 0.12 at 600 °C; the upper bound on conversion is expected to increase with temperature and fall between 97.9% (P = 0.25) and 100% (P = 0.10) [40]. As the calculated values of P become closer to 0.10 with increasing temperatures, near complete conversion of propylene should be expected at relatively high reaction temperatures. However, complete conversion is not observed for propylene oxidation; indeed, this was observed comparing CO and propylene oxidation behavior in experiments. These estimates ignore the aforementioned washcoat diffusion limitations. It can be shown that these limitations decrease the conversion further; quantitative confirmation of this fact will be shown elsewhere [42].

In experiments using the Pd/CZO catalyst, the maximum propylene conversion increases to 98% compared to 93–94% using the other two catalysts. This could be due to the larger pore size of CZO and thus improved washcoat diffusive flux of reactant species compared to Al_2O_3. As noted in Table 1, the average pore size of CZO is roughly twice that of Al_2O_3. In a modeling study to be communicated elsewhere these findings are quantitatively corroborated [42].

4.3. CO + C_3H_6 Co-oxidation

Experiments using both catalysts and a feed mixture of 1% CO and 500 pm C_3H_6 consistently demonstrate that CO light-off occurs at lower temperatures than C_3H_6 light-off. When CO and C_3H_6 are co-fed, the two species competitively adsorb on Pd active sites (i.e. they are mutually inhibiting). CO typically requires one Pd active site per molecule, whereas propylene requires multiple active sites for adsorption and fragmenting into smaller carbonaceous species.

As illustrated in Fig. 12, at the feed concentrations used, Pd active sites will be occupied primarily by CO, which blocks propylene from adsorbing and consequently hinders accumulation of inhibitory carbonaceous species. Oxygen is limited from adsorbing on the surface by both CO and propylene, but adsorbs and dissociates competitively as temperatures increase. As relatively more CO molecules (compared to C_3H_6) are adsorbed on the surface, there is a higher probability of CO reacting with adsorbed oxygen. CO oxidation proceeds and the exothermic nature of the reaction further increases temperatures, increasing the number of active sites for propylene adsorption and oxidation. We confirm and predict these trends elsewhere [42].

4.4. Adiabatic temperature rise

Both CO and propylene oxidation are exothermic reactions and the theoretical temperature rise due to reaction in an adiabatic system, or adiabatic temperature rise (ΔT_{ad}), can be calculated using the following equation:

$$\Delta T_{ad} = \frac{-\Delta H_r y_0 X}{C_{pf}} \quad (22)$$

where ΔH_r is the heat of reaction, y_0 is the feed concentration (mole fraction), X is the conversion, and C_{pf} is the fluid (Argon) heat capacity. The heat capacity of Argon is temperature dependent and based on the Shomate equation [43]. The heats of reaction of CO oxidation and C_3H_6 oxidation are −283 kJ/mol CO and −1925.9 kJ/mol C_3H_6, respectively. Table 8 provides the adiabatic temperature rise assuming complete conversion of feed species for a variety of different fluid temperatures. With increasing fluid temperatures, the

Table 7
Diffusivities and Peclet numbers.

Temperature (°C)	300 °C	400 °C	500 °C	600 °C
D_{CO} (m^2/s)	6.06e-5	7.99e-5	1.01e-4	1.25e-4
D_{C3H6} (m^2/s)	3.54e-5	4.71e-5	6.05e-5	7.50e-5
Pe_{CO}	233	207	188	172
P_{C3H6}	399	351	315	287
P_{CO}	0.10	0.09	0.08	0.07
P_{C3H6}	0.17	0.15	0.13	0.12

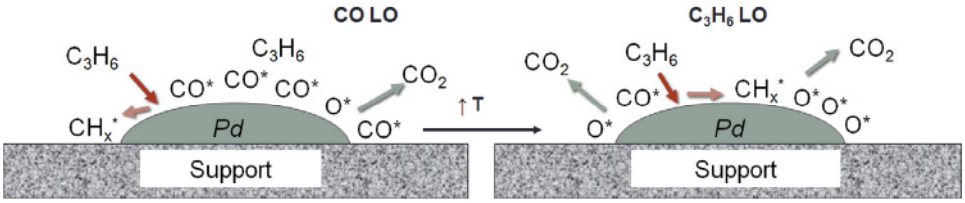

Fig. 12. CO and C_3H_6 order of LO.

Table 8
Adiabatic and Pd/CZO experimental (Expt) temperature rise for select feed temperatures.

Fluid Temperature (°C)	0.5% CO	1% CO	500 ppm C_3H_6
156	65	130 (Expt: 118)	45
178	65 (Expt: 65)	130	44
360	60 (Expt: 41)	120 (Expt: 85)	41
500	55	110	37

expected adiabatic temperature rise decreases. This is due to the fact that the fluid heat capacity increases as fluid temperature increases.

The adiabatic temperature rise is proportional to feed concentration (Eq. (22)); for example, the adiabatic temperature rise for 1% CO is twice that of 0.5% CO for all fluid temperatures. Though the heat of reaction of C_3H_6 oxidation is nearly 7 times greater than that of CO oxidation, the concentrations used in experiments are significantly lower (e.g. 500 ppm is 1/20th of 1%). Accordingly, the adiabatic temperature rise for 500 ppm of C_3H_6 is 37 °C for a fluid temperature of 500 °C, or approximately 7/20th that of the 110 °C adiabatic temperature rise expected for 1% CO at the same fluid temperature.

The estimated adiabatic temperature rise at different fluid feed temperatures is compared to the measured experimental temperature rise as previously shown in Fig. 3. Using the Pd/CZO catalyst to oxidize 1% CO, the temperature difference between monolith middle and feed fluid temperatures is 118 °C for a feed fluid temperature of 156 °C. The experimental temperature rise is similarly lower than the calculated adiabatic temperature rise at a higher feed temperature; for a feed at 360 °C, the observed experimental rise was 85 °C compared to the theoretical 120 °C. The increasing difference between experimental and adiabatic temperature rise could be due to the innate non-adiabatic heat loss within the reactor system. At higher furnace temperatures, there is a higher driving force for heat loss.

5. Conclusions

The oxidations of CO and propylene were studied using model Pd monolith catalysts with Al_2O_3 or CZO supports. CO and propylene were demonstrated to be self-inhibiting and mutually-inhibiting species. The use of zirconia-stabilized ceria in the catalyst washcoat was observed to enhance low temperature CO light-off and propylene oxidation at intermediate and high temperatures. Light-off temperatures and efficiencies during co-oxidation of CO and propylene were also improved using ceria-zirconia in the catalyst compared to behavior using Pd supported on Al_2O_3 alone.

Experiments utilized to derive kinetic parameters including reaction orders and activation energies reveal possible alternate reaction mechanisms for CO and propylene oxidation when enough ceria is present in the catalyst. The reaction order with respect to CO is found to shift from the classic negative first order using Pd/Al_2O_3 to zeroth order using Pd/CZO. Activation energies also decrease using Pd/CZO, suggesting an alternate oxidation pathway and/or lower energy barrier of reaction when enough ceria is available.

Mechanisms are proposed for CO and propylene oxidation on Pd active sites and in the presence of ceria. Ongoing work involves the incorporation of kinetic parameters and mechanistic reaction steps in global and kinetic models to validate experiments trends including LO behavior using catalysts of varying composition, temperature rise during LO, differences in asymptotic conversion limits for CO versus propylene, the lag in conversion during propylene LO, and order of oxidation during mixture LO.

Additional areas of investigation for improved and optimized three-way catalysts include studies using other hydrocarbons (alkenes, aromatics) for a more complete representation of exhaust gas mixtures; aged catalysts to better understand activity and species' oxidation behavior over the full useful life of the three-way catalyst; and, given the insights gleaned from Pd/Al_2O_3 versus Pd/CZO model catalysts, catalysts with varying loading and support composition (e.g. mixed or co-impregnated Al_2O_3 and CZO supports).

Acknowledgements

The work reported was funded by Ford Motor Company. The authors appreciate the suggestions from Dr. Robert McCabe (now with NSF) and Dr. Manish Sharma (now with BASF).

References

[1] H.S. Gandhi, G.W. Graham, R.W. McCabe, J. Catal. 216 (2003) 433.

[2] X. Chen, Y. Cheng, C.Y. Seo, J.W. Schwank, R.W. McCabe, Appl. Catal. B: Environ. 163 (2015) 499.
[3] M.V. Twigg, Catal. Today 163 (2011) 33.
[4] A. Russell, W.S. Epling, Catal. Rev.: Sci. Eng. 53 (2011) 337.
[5] M. Hiettiko, U. Lassi, K. Kallinen, A. Savimaki, M. Harkonen, J. Pursiainen, R.S. Laitnen, R.L. Keiski, Appl. Catal. A: Chem. 277 (2004) 107.
[6] R.J. Gorte, AIChE J. 56 (2010) 1126.
[7] T. Bunluesin, R.J. Gorte, G.W. Graham, Appl. Catal. B.: Environ. 14 (1997) 105.
[8] M. Fernandez-Garcia, A. Martinez-Arias, A. Iglesias-Juez, A.B. Hungria, J.A. Anderson, J.C. Conesa, J. Soria, Appl. Catal. B: Environ. 31 (2001) 39.
[9] A. Trovarelli, Catal. Rev.: Sci. Eng. 38 (1996) 439.
[10] A. Martinez-Arias, M. Fernandez-Garcia, A. Iglesias-Juez, A.B. Hungria, J.A. Anderson, J.C. Conesa, J. Soria, Appl. Catal. B: Environ. 31 (2001) 51.
[11] M. Cargnello, V.V.T. Doan-Nguyen, T.R. Gordon, R.E. Diaz, E.A. Stach, R.J. Gorte, P. Fornaseira, C.B. Murray, Science 341 (2013) 771.
[12] M.J. Patterson, D.E. Angove, N.W. Cant, Appl. Catal. B: Environ. 26 (2000) 47.
[13] T. Maillet, C. Solleau, J. Barbier Jr., D. Duprez, Appl. Catal. B.: Environ. 14 (1997) 85.
[14] M.-F. Luo, Z.-Y. Hou, X.-X. Yuan, X.-M. Zheng, Catal. Lett. 50 (1998) 205.
[15] Y.-F.Y. Yao, J. Catal. 87 (1984) 152.
[16] G.S. Zafaris, R.J. Gorte, J. Catal. 143 (1993) 86.
[17] S.H. Oh, C.C. Eickel, J. Catal. 112 (1988) 543.
[18] T. Bunleusin, H. Cordatos, R.J. Gorte, J. Catal. 157 (1995) 222.
[19] S. Sharma, M.S. Hegde, R.N. Das, M. Pandey, Appl. Catal. A: Environ. 337 (2008) 130.
[20] M. Fernandez-Garcia, A. Iglesias-Juez, A. Martinez-Arias, A.B. Hungria, J.A. Anderson, J.C. Conesa, J. Soria, J. Catal. 221 (2004) 594.
[21] J.M.A. Harmsen, H.B.J. Hoebink, J.C. Shouten, Chem. Eng. Sci. 56 (2001) 2019.
[22] J.R. Gonzalez-Velasco, J.A. Botas, J.A. Gonzalez-Marcos, M.A. Gutierrez-Ortiz, Appl. Catal. B: Environ. 12 (1997) 61.
[23] T.A. Nijhuis, A.E.W. Beers, T. Vergunst, I. Hoek, F. Kapteijn, J.A. Moulijn, Catal. Rev. 42 (2001) 345.
[24] R.S. Monteiro, L.C. Dieguez, M. Schmal, Catal. Today 56 (2001) 77.
[25] N.W. Cant, P.C. Hicks, B.S. Lennon, J. Catal. 54 (1978) 372.
[26] D.R. Rainer, M. Koranne, S.M. Vesecky, D.W. Goodman, J. Phys. Chem. B 101 (1997) 10769.
[27] D.W. Goodman, C.H.F. Peden, J. Phys. Chem. 90 (1986) 4839.
[28] N.W. Cant, W.K. Hall, J. Catal. 16 (1970) 220.
[29] Y. Mooroka, A. Ozaki, J. Catal. 5 (1966) 116.
[30] K.I. Choi, M.A. Vannice, J. Catal. 131 (1991) 1.
[31] J. Wang, H. Chen, Z. Hu, M. Yao, Y. Li, Catal. Rev. 57 (2015) 79.
[32] C. Becker, C.R. Henry, Surf. Sci. 353–354 (1996) 457.
[33] P.J. Berlowitz, C.H.F. Peden, D.W. Goodman, J. Phys. Chem. 92 (1988) 5213.
[34] E. Bekyrayova, P. Fornaseiro, J. Kaspar, M. Graziani, Catal. Today 45 (1998) 179.
[35] T. Bunleusin, E.S. Putna, R.J. Gorte, Catal. Lett. 41 (1996) 1.
[36] Y. Cheng, R.W. McCabe, Ford Motor Company, Private Communication, 2014.
[37] S.E. Oh, G.B. Fisher, J.E. Carpenter, D.W. Goodman, J. Catal. 100 (1986) 360.
[38] M.J. Hazlett, M. Moses-Debusk, J.E. Parks II, L.F. Allard, W.S. Epling, Appl. Catal. B.: Environ. 202 (2017) 404.
[39] H. Steinginger, H. Ibach, S. Lehwald, Surf. Sci. 117 (1982) 685.
[40] V. Balakotaiah, D.H. West, Chem. Eng. Sci. 57 (2002) 1269.
[41] R. Raj, M.P. Harold, V. Balakotaiah, Chem. Eng. J. 281 (2015) 322.
[42] W. Lang, P. Laing, Y. Cheng, C. Hubbard, M.P. Harold, in preparation (2017).
[43] NIST Webbook, Gas phase thermochemistry data: Argon (1982).